Published in "Biomedical Optics Express 6(7): 2552, 2015"
which should be cited to refer to this work.

Subsurface ablation of atherosclerotic plaque using ultrafast laser pulses

Thomas Lanvin,[1] Donald B. Conkey,[1] Aurelien Frobert,[2] Jeremy Valentin,[2] Jean-Jacques Goy,[2] Stéphane Cook,[2] Marie-Noelle Giraud,[2] and Demetri Psaltis[1,*]

[1] *Optics Laboratory, École Polytechnique Fédérale de Lausanne, 1015 Lausanne, Switzerland*
[2] *Cardiology, Department of Medicine, University of Fribourg, 1700 Fribourg, Switzerland*
[*] *demetri.psaltis@epfl.ch*

Abstract: We perform subsurface ablation of atherosclerotic plaque using ultrafast pulses. Excised mouse aortas containing atherosclerotic plaque were ablated with ultrafast near-infrared (NIR) laser pulses. Optical coherence tomography (OCT) was used to observe the ablation result, while the physical damage was inspected in histological sections. We characterize the effects of incident pulse energy on surface damage, ablation hole size, and filament propagation. We find that it is possible to ablate plaque just below the surface without causing surface damage, which motivates further investigation of ultrafast ablation for subsurface atherosclerotic plaque removal.

References and links

1. J. A. Finegold, P. Asaria, and D. P. Francis, "Mortality from ischaemic heart disease by country, region, and age: Statistics from World Health Organisation and United Nations," Int. J. Cardiol. **168**(2), 934–945 (2013).
2. V. Fuster, P. R. Moreno, Z. A. Fayad, R. Corti, and J. J. Badimon, "Atherothrombosis and High-Risk Plaque: Part I: Evolving Concepts," J. Am. Coll. Cardiol. **46**(6), 937–954 (2005).
3. G. R. Mood, MD, J. Lee, MD, PhD, L. A. Garcia, MD, "Atherectomy in the Treatment of Lower-Extremity Peripheral Artery Disease: A Critical Review | Vascular Disease Management," http://www.vasculardiseasemanagement.com/content/atherectomy-treatment-lower-extremity-peripheral-artery-disease-critical-review.
4. P. C. Block, J. T. Fallon, and D. Elmer, "Experimental angioplasty: lessons from the laboratory," AJR Am. J. Roentgenol. **135**(5), 907–912 (1980).
5. R. Ginsburg, L. Wexler, R. S. Mitchell, and D. Profitt, "Percutaneous transluminal laser angioplasty for treatment of peripheral vascular disease. Clinical experience with 16 patients," Radiology **156**(3), 619–624 (1985).
6. J. A. Bittl, T. A. Sanborn, J. E. Tcheng, R. M. Siegel, and S. G. Ellis, "Clinical success, complications and restenosis rates with excimer laser coronary angioplasty," Am. J. Cardiol. **70**(20), 1533–1539 (1992).
7. D. L. Singleton, G. Paraskevopoulos, R. Taylor, and L. Higginson, "Excimer laser angioplasty: Tissue ablation, arterial response, and fiber optic delivery," IEEE J. Quantum Electron. **23**(10), 1772–1782 (1987).
8. S. L. Trokel, R. Srinivasan, and B. Braren, "Excimer laser surgery of the cornea," Am. J. Ophthalmol. **96**(6), 710–715 (1983).
9. X. Liu, D. Du, and G. Mourou, "Laser ablation and micromachining with ultrashort laser pulses," IEEE J. Quantum Electron. **33**(10), 1706–1716 (1997).
10. C. V. Gabel, "Femtosecond lasers in biology: nanoscale surgery with ultrafast optics," Contemp. Phys. **49**(6), 391–411 (2008).
11. C. L. Hoy, O. Ferhanoglu, M. Yildirim, K. H. Kim, S. S. Karajanagi, K. M. C. Chan, J. B. Kobler, S. M. Zeitels, and A. Ben-Yakar, "Clinical Ultrafast Laser Surgery: Recent Advances and Future Directions," IEEE J. Sel. Top. Quantum Electron. **20**(2), 242–255 (2014).
12. D. Du, X. Liu, G. Korn, J. Squier, and G. Mourou, "Laser-induced breakdown by impact ionization in SiO2 with pulse widths from 7 ns to 150 fs," Appl. Phys. Lett. **64**(23), 3071–3073 (1994).
13. A. Vogel, S. Busch, and U. Parlitz, "Shock wave emission and cavitation bubble generation by picosecond and nanosecond optical breakdown in water," J. Acoust. Soc. Am. **100**(1), 148–165 (1996).
14. A. Vogel, J. Noack, G. Hüttman, and G. Paltauf, "Mechanisms of femtosecond laser nanosurgery of cells and tissues," Appl. Phys. B **81**(8), 1015–1047 (2005).

15. M. Cilingiroglu, J. H. Oh, B. Sugunan, N. J. Kemp, J. Kim, S. Lee, H. N. Zaatari, D. Escobedo, S. Thomsen, T. E. Milner, and M. D. Feldman, "Detection of vulnerable plaque in a murine model of atherosclerosis with optical coherence tomography," Catheter. Cardiovasc. Interv. **67**(6), 915–923 (2006).
16. K. S. Meir and E. Leitersdorf, "Atherosclerosis in the Apolipoprotein-E-Deficient Mouse: A Decade of Progress," Arterioscler. Thromb. Vasc. Biol. **24**(6), 1006–1014 (2004).
17. Y. Nakashima, A. S. Plump, E. W. Raines, J. L. Breslow, and R. Ross, "ApoE-deficient mice develop lesions of all phases of atherosclerosis throughout the arterial tree," Arterioscler. Thromb. **14**(1), 133–140 (1994).
18. M. H. Niemz, "Threshold dependence of laser-induced optical breakdown on pulse duration," Appl. Phys. Lett. **66**(10), 1181–1183 (1995).
19. J. Nguyen, J. Ferdman, M. Zhao, D. Huland, S. Saqqa, J. Ma, N. Nishimura, T. H. Schwartz, and C. B. Schaffer, "Sub-surface, micrometer-scale incisions produced in rodent cortex using tightly-focused femtosecond laser pulses," Lasers Surg. Med. **43**(5), 382–391 (2011).
20. C. Xu, J. M. Schmitt, S. G. Carlier, and R. Virmani, "Characterization of atherosclerosis plaques by measuring both backscattering and attenuation coefficients in optical coherence tomography," J. Biomed. Opt. **13**(3), 034003 (2008).
21. F. J. van der Meer, D. J. Faber, D. M. Baraznji Sassoon, M. C. Aalders, G. Pasterkamp, and T. G. van Leeuwen, "Localized measurement of optical attenuation coefficients of atherosclerotic plaque constituents by quantitative optical coherence tomography," IEEE Trans. Med. Imaging **24**(10), 1369–1376 (2005).
22. J. L. Suhalim, C.-Y. Chung, M. B. Lilledahl, R. S. Lim, M. Levi, B. J. Tromberg, and E. O. Potma, "Characterization of Cholesterol Crystals in Atherosclerotic Plaques Using Stimulated Raman Scattering and Second-Harmonic Generation Microscopy," Biophys. J. **102**(8), 1988–1995 (2012).
23. R. Kammel, R. Ackermann, A. Tünnermann, and S. Nolte, "Pump-probe investigation of fs-LIOB in water by simultaneous spatial and temporal focusing," in (2013), Vol. 8611, p. 86110A–86110A–7.
24. M. Miclea, U. Skrzypczak, S. Faust, F. Fankhauser, H. Graener, and G. Seifert, "Nonlinear refractive index of porcine cornea studied by z-scan and self-focusing during femtosecond laser processing," Opt. Express **18**(4), 3700–3707 (2010).
25. H. Wisweh, U. Merkel, A.-K. Hüller, K. Lüerßen, and H. Lubatschowski, "Optical coherence tomography monitoring of vocal fold femtosecond laser microsurgery," in (2007), Vol. 6632, pp. 663207–663207–7.
26. W. M. Suh, A. H. Seto, R. J. P. Margey, I. Cruz-Gonzalez, and I.-K. Jang, "Intravascular Detection of the Vulnerable Plaque," Circ Cardiovasc Imaging **4**(2), 169–178 (2011).
27. Y. Wang, M. Alharbi, T. D. Bradley, C. Fourcade-Dutin, B. Debord, B. Beaudou, F. Gerôme, and F. Benabid, "Hollow-core photonic crystal fibre for high power laser beam delivery," High Power Laser Sci. Eng. **1**(01), 17–28 (2013).
28. Y. Y. Wang, X. Peng, M. Alharbi, C. F. Dutin, T. D. Bradley, F. Gérôme, M. Mielke, T. Booth, and F. Benabid, "Design and fabrication of hollow-core photonic crystal fibers for high-power ultrashort pulse transportation and pulse compression," Opt. Lett. **37**(15), 3111–3113 (2012).
29. O. Ferhanoglu, M. Yildirim, K. Subramanian, and A. Ben-Yakar, "A 5-mm piezo-scanning fiber device for high speed ultrafast laser microsurgery," Biomed. Opt. Express **5**(7), 2023–2036 (2014).
30. Z. Qian, A. Mordovanakis, J. E. Schoenly, A. Covarrubias, Y. Feng, L. Lilge, and R. S. Marjoribanks, "Pulsetrain-burst mode, ultrafast-laser interactions with 3D viable cell cultures as a model for soft biological tissues," Biomed. Opt. Express **5**(1), 208–222 (2014).

1. Introduction

Each year more than 7 million people die from coronary heart disease (CHD), making it the most common cause of death worldwide [1]. Coronary artery disease, the main cause of CHD, develops as immune cells and lipids accumulate in plaques inside the coronary arterial wall. As a plaque grows, the tissue layer (fibrous cap) separating it from the blood flow becomes thinner. When the fibrous cap becomes less than 65 microns thick the plaque is considered vulnerable [2]. The consequent narrowing of the artery or a sudden plaque rupture through the thin fibrous cap leads to an ischemic event and myocardial infarction that may be lethal. Prevention of ischemic events is a major unsolved medical issue that requires the stabilization and/or treatment of the so-called vulnerable plaque. Atherectomy, or the removal of plaque from arteries, has long been studied and clinically utilized as a treatment of atherosclerosis [3]. The first attempts to remove atherosclerotic plaque with laser ablation date back to the 1970s. These initial experiments relied on thermal effects produced by the linear absorption of a continuous wave (CW) laser beam [4]. However, the ablation charred surrounding tissue which complicated healing with restenosis (re-narrowing of the artery) [5]. These results led to the abandonment of CW laser use for atherectomy, and the initiation of research with pulsed lasers in the mid-1980s [6,7]. The laser atherectomy methods commercialized in the last 10 years are based on the ultraviolet excimer laser with nanosecond pulses. Although the

shorter pulse duration mitigates long range thermal effects, these lasers also rely on linear absorption and thus were not fit for subsurface ablation [8]. Consequently, their use is limited to the extremities of the body where plaque rupture is less life threatening [7].

Here we demonstrate that ablation with ultrafast pulses (duration less than 10 ps) provides a mechanism to vaporize plaque without damaging the surface. Ultrafast ablation has proven useful in high-precision manufacturing [9] and has a great potential for biomedical microsurgery [10,11]. The high intensity of a focused ultrafast pulse enables nonlinear absorption of the laser energy which three-dimensionally confines the interaction to the focal volume [12]. Ultrafast ablation occurs when laser irradiance surpasses an optical breakdown threshold over which multiphoton ionization leads to plasma formation [13]. In this process most of the additional pulse energy feeds the rapidly growing plasma, thus minimizing heat accumulation and thermal damage beyond the focal volume. Additionally, a cavitation bubble forms with the expansion of material vaporized during this process. The result is a highly confined ablation region and a lingering volume of gas containing the remnants of the ablated volume that eventually diffuses into the surrounding tissue [14].

In the present paper we describe the results of an *ex vivo* investigation of the structural damage caused by ultrafast ablation in atherosclerotic plaque and neighboring arterial tissue of a mice model of atherosclerosis. We characterize the ablated tissue to present an overall assessment of the structural damage achievable within our experimental parameters. We monitor the ablation using optical coherence tomography (OCT), an imaging modality commonly used to characterize atherosclerotic plaques [15]. The main result we report is that it is possible to ablate the plaque just below the surface of the artery without damaging the surface tissue.

2. Experimental methods

The ablation experiments were performed using aortas extracted from genetically engineered mice that lack the apolipoprotein E (ApoE) gene [16]. The ApoE knock-out (ApoE-KO) mice developed atherosclerotic plaques, particularly in the ascending aorta and the aortic arch when fed with a lipid-rich diet. In ApoE-KO mice, the plaques typically develop within the tunica intima just a few microns below the endothelium of the arterial wall and grow to a couple hundred microns thick (see Fig. 1 for an illustration). The plaques have a similar composition to human plaque with a fatty deposit and a thin fibrous cap [17]. Six animals were fed for 12 to 16 weeks with a lipid-rich diet (0.2% cholesterol and 21% butter, Western U8958 version 35, SAFE, France). The mice were anesthetized and sacrificed prior to aorta harvesting and kept in phosphate buffer saline (PBS) solution on ice. Within 2 to 5 hours after harvesting, the arteries were cut open along the longitudinal axis, immersed in PBS solution, and mounted on a microscope slide with a cover slide. The tissues were then subjected to laser ablation with illumination from the endothelial side. All animals received humane care in compliance with the European Convention on Animal Care and in accordance with the Swiss Animal Protection Law after obtained permission of the State Veterinary Office, approved by the Swiss Federal Veterinary Office, Switzerland (FR 2013/35).

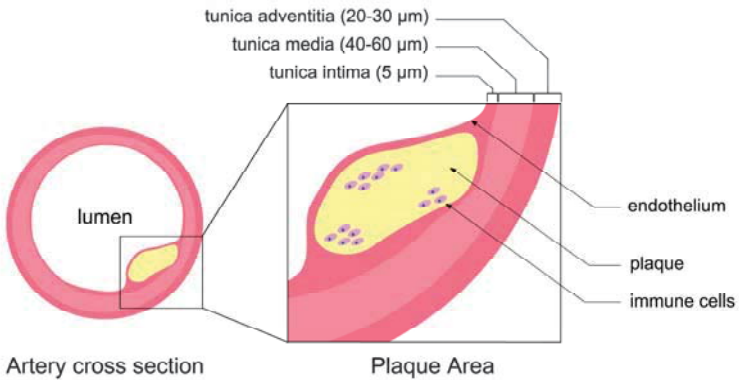

Fig. 1. A cross sectional view of an artery illustrating the location of plaque and the arterial layers.

An optical apparatus was built for ultrafast ablation and observation (Fig. 2(a)). A compact 1030nm, 20W fiber laser (Satsuma HP2, Amplitude Systèmes) with tunable pulse width, repetition rate, and pulse energy provided high-energy, ultrafast laser input to the system. A 1.5 ps pulse duration, was selected to mitigate nonlinear self-focusing effects [11] while having ablation threshold values similar to femtosecond pulses [18]. The repetition rate was set to 1 kHz, sufficiently low to avoid pulse to pulse heat accumulation [19]. The laser beam was collimated and expanded to fill the back aperture of a water immersion, long working distance objective (Nikon NIR APO 40X, NA 0.8) mounted in an upright position. The objective focused the beam to a focal spot (FWHM of 0.8 μm transverse and 1 μm axial) on the sample, which was mounted on a 3-axis piezo mechanical stage. Two complementary imaging systems were integrated into the apparatus to monitor the target area: (1) a CCD camera provided a widefield image of the target area via a removable beamsplitter and (2) a spectral domain OCT system (Thorlabs, Ganymede) was used to observe the same sample area from the posterior side (the tunica adventitia side, see Fig. 1). The OCT enabled depth visualization of the ablated tissue. The laser parameters, the stage motion, and both observation systems were controlled by computer.

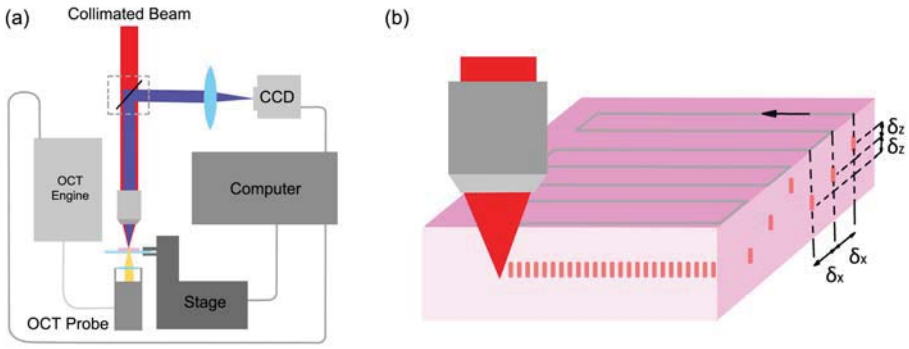

Fig. 2. (a) Schematic of the ablation set-up. An objective (NA 0.8) focused the collimated ultrafast pulses into the tissue mounted on the x,y,z stage. A computer controlled the CCD, OCT, and mechanical stage. The beam splitter directing the reflected light (blue) toward the CCD was removed during ablation. (b) Representation of the serpentine ablation pattern. Each line was separated transversely by δ_x and axially by δ_z. For all experiments the arterial endothelium was placed toward the incident laser pulse.

To facilitate ablation analysis, a specific ablation pattern was implemented by movement of the mechanical stage. The velocity of the stage was adjusted to $v = (1 - n)df$, where d is the spot size of the focused laser illumination, f is the laser pulse repetition rate, and n is the percentage overlap between subsequent pulses that was set between 0 and 0.8. The ablation pattern routine created 8 or 10 ablation lines, each line separated in the transverse (x) direction by $\delta_x = 30$ μm and in the axial (z) direction by $\delta_z = 10$ or $\delta_z = 15$ μm (Fig. 2(b)). The number of lines and δ_z were selected to allow for ablation from the endothelium, through the plaque, and into the tunica media. The focusing depth was at most 150 μm, which placed most ablation holes within the photon scattering mean free path of plaque (50 to 200 μm in near infrared (NIR)) [20–22]. Thus, attenuation of the focused pulse was minimal within the ablation depth range and deeper ablation was prohibited by the thickness of tissue samples.

To preserve the ablation holes for analysis, the ablated tissue samples were frozen and prepared for histologic sectioning. A time greater than the observed gas bubble diffusion time (~30 min) elapsed following the ablation to ensure measurement of ablation hole size and not gas bubble size. The samples were then removed from the slide and immersed into cryogenic matrix (Cryomatrix, Thermo Scientific) and slowly frozen to –20°C in the fumes of isopentane cooled by dry ice. Later, the samples were cut orthogonal to the ablation lines into 8 μm sections using a cryocut and stained with haematoxylin and eosin (H&E).

3. Ablation characterization metrics

The H&E stained histological sections were evaluated under a transmission widefield microscope with a 40x objective (NA 0.7). Figures 3(a)-3(e) portray a variety of holes created with the ultrafast laser ablation. These holes range from well-defined symmetric holes of about 5 μm diameter (Fig. 3(a), E = 0.6 μJ) to elongated damage up to 100 μm in length (Fig. 3(d), E = 10 μJ) depending on the pulse energy used. Figure 3(f) details the metrics used for the hole assessment: the depth of ablation, D, the transverse and axial extent of the ablation hole, R_b and L_b, and the total length of ablation including a damage tail, L_r (Fig. 3(b)-3(d)). Figure 3(g) is a representative tissue section showing the ablation pattern illustrated in Fig. 2(b). For an accurate assessment of subsurface ablation width, it was necessary to filter out results from scenarios in which the laser was focused on the surface of the tissue and surface damage was expected. Thus, only ablation holes that were deeper than 10 μm were considered in the ablation width analysis, as the axial length of the ablation damage was ~10 μm.

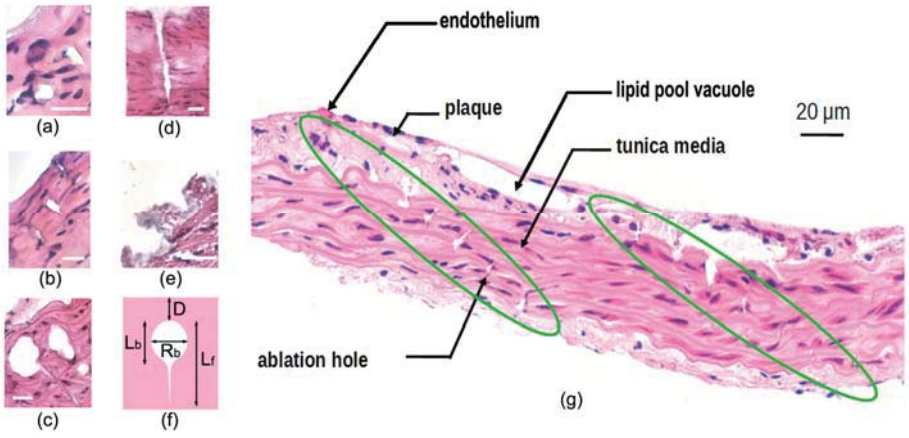

Fig. 3. Images of ablation holes from histological slices. (a) 5 μm ablation spot (E = 0.6 μJ), (b) 5 μm ablation spot with short filamentation (E = 0.6 μJ), (c) ablation spot with elongated filamentation tail (E = 4 μJ), (d) long filamentation (E = 10 μJ), (e) surface damage (E = 4 μJ), (f) Schematic describing how the different holes were characterized, (g) representative ablation pattern marked within green ovals (E = 4 μJ). Scale bar is 10 μm in (a)-(e).

The evaluation of the ablated tissue revealed that high energy pulses tended to yield elongated, thin ablation structures. Although other optical effects may play a role, we believe the elongation is primarily caused by self-trapping of the ablation beam, which results from a nonlinear optical effect in which high optical power induces a local refractive index change that refocuses the beam and propagates as a filament [23]. We observed the elongated damage with multiple repeated pulses but also with single pulse ablation (pulse overlap, $n = 0$). Therefore we infer that the elongation was not a result of cumulative pulse-to-pulse effects. Furthermore, the optical powers used were in the range of the expected self-focusing critical power for biological tissue [24]. In the remainder of the paper we refer to the thin, elongated structural damage as filament damage. For the analysis filamentation was considered to be present in either of two cases: (1) a tail of structural damage was apparent in the sample which continued from the ablated volume deeper into the tissue (Fig. 3(b) and 3(c)), or (2) the aspect ratio of the ablation hole was 0.2 or less (Fig. 3(d)), corresponding to an axial dimension greater than five times its transverse diameter. In the second case, the filamentation length, L_r, was set to the axial dimension of the hole, L_b, to be consistent with the measurement method presented in Fig. 3(f).

4. Ablation characterization results

The structural damage from ultrafast ablation in both plaque and the neighboring tunica media were characterized. Several criteria of the ablation holes were assessed, including the surface damage, the ablation width, the ablation difference in plaque and tunica media, and filament propagation. All of these were analyzed in relation to incident pulse energy. No significant difference was seen within the range of pulse overlap values or in ablation size dependence on depth. 2106 holes were individually characterized from the atherosclerotic aortas of the ApoE-KO mice.

To understand the surface damage risk of ultrafast ablation, we analyzed its dependence on pulse energy and ablation depth in plaque. The existence of surface damage was evaluated on whether any structural modification existed above an ablation hole and near the surface of the tissue sample (<10 μm). This damage could be observed by visual inspection of the histological section as a structural deformation near the surface of the artery (see Fig. 3(b)). If an ablation hole extended all the way to the surface the damage was also clearly visible (see Fig. 3(d) and 3(e)). Figure 4(a) plots the percentage of ablation holes with surface damage as a function of pulse energy in three different depth ranges. As expected, the likelihood of surface damage decreases with increasing depth and decreasing energy. The results indicate that the risk of surface damage is minimal when focusing deeper than 15 μm under the surface with pulse energies below 4 μJ. Importantly, this suggests the possibility of ablating unstable plaques without damaging thin fibrous caps.

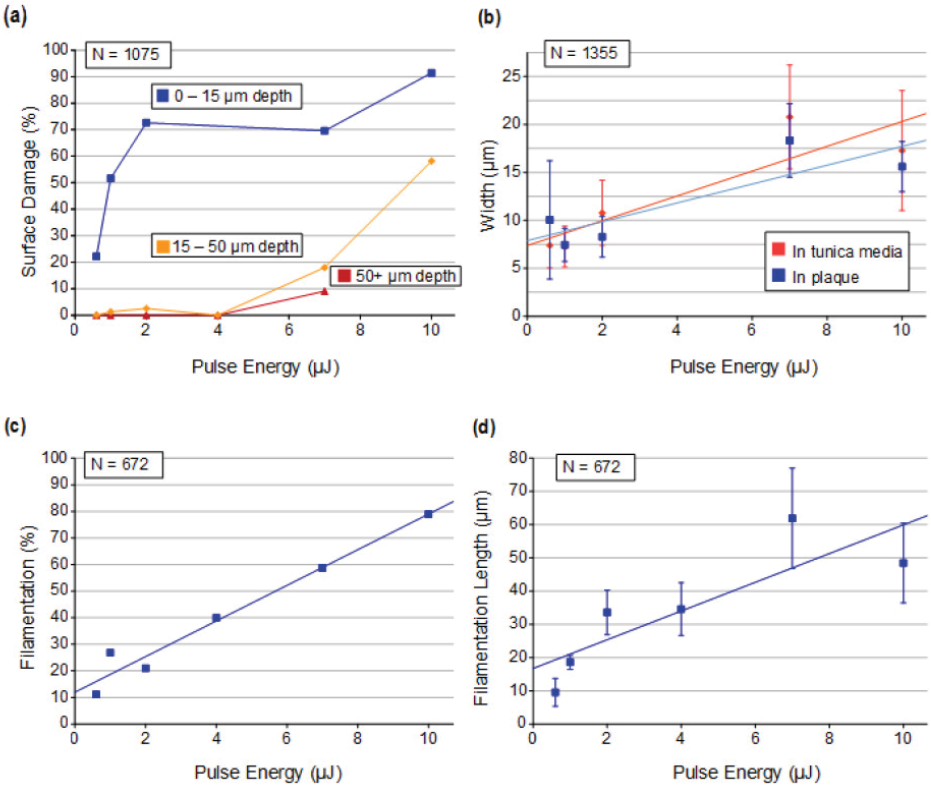

Fig. 4. Characterization results of ultrafast ablation. N is the number of holes characterized. (a) The percentage of ablation holes with surface damage as a function of pulse energy for three depth ranges. (b) Transverse ablation width measured in plaque and tunica media versus pulse energy. (c) The percentage of holes with filament tails as a function of pulse energy. (d) Filament propagation length versus pulse energy.

The transverse size of the ablation hole depends weakly on the pulse energy and depth. Specifically, in the range of 0.6 - 2 µJ and within the 150 µm depth we obtain approximately 10 µm ablation hole width (Fig. 4(b)). In addition, no significant differences were found between the size of the ablation holes in plaque and tunica tissue (Fig. 4(b)). The transversal ablation width marginally increased with the pulse energy and remained within cellular dimensions (<30 µm). On the other hand, higher pulse energy significantly increased the axial extent of the ablation damage due to filament formation. The filament propagation in plaque was characterized in two ways: (1) the percentage of holes exhibiting filament formation (Fig. 4(c)) and (2) the filament propagation length (Fig. 4(d)). The likelihood of filamentation showed a linear dependence on pulse energy and increased from 10% at 0.6 µJ pulse energy to 80% at 10 µJ pulse energy. Only pulse energies below 1 µJ limited filament propagation to sub-cellular lengths, while filaments formed with 10 µJ pulse energy extended on average 50 µm.

5. OCT observation of ultrafast ablation

The objective of a second experiment was to ablate an extended volume of tissue and image it with OCT. The high refractive index difference between gas and tissue is well suited for OCT imaging. OCT has been previously used to observe subsurface vapor bubbles originating from ablation in excised porcine vocal folds [25]. In the case of atherosclerotic plaque, it can be used to both locate the plaque and monitor the ablation.

An initial test to image bulk subsurface ablation with OCT in a non-atherosclerotic mouse aorta (obtained from a C57/BL/6 mouse) was pursued. For bulk material ablation, a pattern similar to Fig. 2(b) was implemented with δ_x = 5 μm and δ_z = 0 μm to ablate in a single plane parallel to the tissue surface. The pattern resulted in an ablated plane of area 100x200 μm^2, as opposed to the discrete lines of the first experiment. Using a stage scanning speed with a pulse to pulse overlap of n = 0.8, this pattern could be scanned in 280 ms. The actual scanning time was somewhat longer due to corner turning delays. The pattern was ablated with 1 μJ pulses targeting 50 μm deep in the tunica media. An OCT image acquired a few seconds after ablation showed that the parallel ablation lines were dense enough to create a 30 μm thick, gas filled volume in the entire scanned area. After OCT imaging, the sample was frozen and prepared for histological sectioning following the procedure described previously. In the ablated region, the right side of the hole had collapsed in both the OCT image (Fig. 5(a)) and histological section (Fig. 5(b)). In general there is excellent agreement between the OCT and histology images. Corroborating our results, there was no observable surface damage and negligible filamentation at this pulse energy. Furthermore, the ablation area appears clearly defined, without detectable structural damage outside the target area.

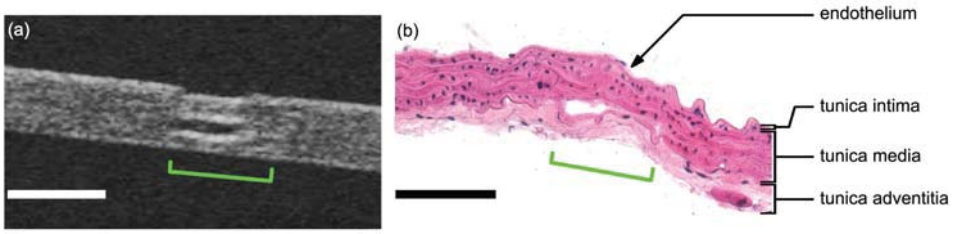

Fig. 5. Tunica media of non-atherosclerotic mouse aorta ablated with a 100x200 μm^2 plane. (a) Transverse OCT image of the ablation area. (b) Transverse histological cut of the ablation area. The green brackets refer to the extent of the ablation plane. The images are oriented in the same direction. The incident ablation pulse comes from the endothelium side.

Finally, subsurface ablation of plaque was performed and the resulting vapor bubble evolution monitored via OCT. For this demonstration the plaque was discernible with OCT and was specifically targeted for ablation. Five planes were consecutively ablated one above another, beginning with the deepest plane and moving towards the endothelium. By using 1 μJ pulse energy and selecting a separation of 10 μm between each plane, an ablation volume of 100x200x50 μm^3 was targeted. The sample, a 25 week old ApoE-KO mouse, provided a thick plaque (up to 400 μm) with a large lipid core and a thick fibrous cap. The sample was placed in an imaging chamber (CoverWell, Grace Bio-Labs). The plaque thickness required that the tissue sample be flipped over for OCT observation following the ablation procedure. Transversal OCT images of the region at 1, 3, and 5 minutes after ablation were obtained and the histological sections were stained with H&E for an assessment of surface damage (Fig. 6). The post-ablation OCT image showed that the gas bubble was clearly confined 40 μm below the surface (Fig. 6(a)). Despite the relatively large volume targeted, the gas bubble volume after 1 minute was 70x160x33 μm^3 and no bubble could be observed after 5 minutes (Fig. 6(b)-6(d) for 1, 3, and 5 minutes after ablation). The corresponding histological slice (Fig. 6(e)) showed that there was no structural damage within 40 μm of the surface and that we mainly targeted the lipid core of the plaque. In this demonstration, OCT imaging facilitated subsurface, plaque-specific ablation and monitoring of the post-ablation gas bubble dynamics within the tissue.

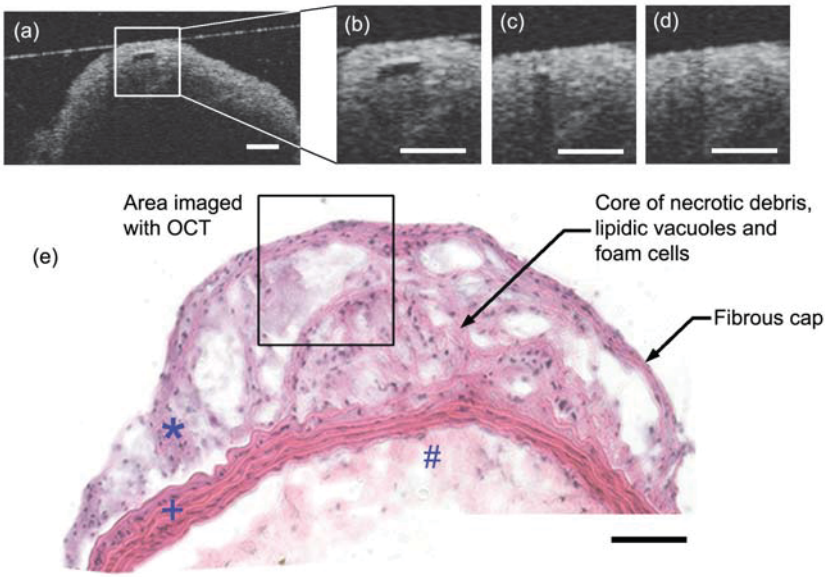

Fig. 6. ApoE-KO mouse plaque after ablation of a 100x200x50 μm^3 targeted volume. (a) Transverse OCT image of the ablation area. (b-d) Time evolution of the ablated volume after the ablation (t = 0 min). (b) t = 1 min, (c) t = 3 min, (d) t = 5 min. (e) Transverse of the histological cut of the ablation area. (*) plaque, (+) tunica media, (#) tunica adventitia. All scale bars are 100 µm. The incident ablation pulse comes from the plaque side.

6. Discussion

We have characterized ultrafast ablation in atherosclerotic plaque and tunica media tissue. OCT provided high contrast images of the gas bubble resulting from ablation. Since IV-OCT devices already exist and provide clinicians a valuable, high-resolution tool for plaque recognition and characterization [26] a method for monitoring ultrafast ablation is readily available for a clinical setting. The study indicated that ultrafast ablation in plaque and the tunica media have similar characteristics regardless of the energy levels we experimented with. The results further indicated that pulse energies below 4 µJ provided axially isolated ablation volumes, such that ablation targeted deeper than 15 µm rarely induced surface damage. These results suggest the possibility of the fine ablation of unstable plaques only a few tens of microns beneath the endothelium. The experiment also revealed that filament propagation plays an important role in ultrafast ablation of plaques with the studied experimental parameters. The measurements we have presented would be used in the design of a catheter device to balance the effects of filamentation and ablation width in plaques.

The applicability of these results for a minimally-invasive catheter approach also depends on the ability to transfer the laser pulses through optical fibers. Fortunately, in the last decade there has been consistent progress in the maximum peak power which can propagate through single-mode hollow core photonic crystal fibers (HC-PCF) [27]. Picosecond pulses with energies of several tens of microjoules have been transmitted through large mode area HC-PCFs [28]. In fact, ultrafast ablation has recently been demonstrated using HC-PCFs for pulse delivery with a catheter device [29].

In regards to future work, several experiments could be pursued. A study to understand the range of the collateral cellular damage and reaction to ultrafast ablation would be informative because cell damage or death can extend beyond the ablation hole and result in either necrotic or apoptotic cell death [30]. As plaque vulnerability is effected by multiple processes, understanding the effect of ultrafast ablation on these factors, such as plaque

composition, should also be pursued. Also, studying the long-term effects, such as inflammation and other immune responses, is necessary to understanding the medical implications of this approach. Of course, this study would require *in vivo* testing for which a catheter prototype would be most appropriate.

7. Conclusion

We have presented the initial steps towards the use of ultrafast ablation for atherosclerotic plaque treatment. The experiments were performed on the atherosclerotic aortas of ApoE-KO mice. We demonstrated that plaque can be ablated just below the endothelial surface without damaging the surface tissue layers. The ablation process was observed with OCT, which provided high-resolution, high-contrast images of the gas volume resulting from ablation. Further development of a catheter device will provide additional insight into the feasibility of subsurface treatment of atherosclerotic plaque with ultrafast, high-energy laser pulses.

Acknowledgments

We thank Thorlabs for lending the Ganymede OCT system. We acknowledge the support provided by the EPFL Histology Core Facility. D.B.C. acknowledges support from the 'EPFL Fellows' fellowship program co-funded by Marie Curie, FP7 Grant agreement no. 291771.